ELSEVIER

Materials Science and Engineering A 454–455 (2007) 260–265

MATERIALS SCIENCE & ENGINEERING A

www.elsevier.com/locate/msea

Microstructure and compressive properties of multicomponent $Al_x(TiVCrMnFeCoNiCu)_{100-x}$ high-entropy alloys

Y.J. Zhou *, Y. Zhang, Y.L. Wang, G.L. Chen

State Key Laboratory for Advanced Metals and Materials, University of Science and Technology Beijing, Beijing 100083, China

Received 2 October 2006; received in revised form 3 November 2006; accepted 7 November 2006

Abstract

The microstructure and compressive properties of $Al_x(TiVCrMnFeCoNiCu)_{100-x}$ ($x = 0$, 11.1, 20 and 40 at.%) high-entropy alloys were studied. With the increase of Al content, the number of phases in the alloys gradually decreases. When Al content is 20 at.%, only bcc solid-solution structure is found in the alloy. The effect of high mixing entropy does facilitate the formation of simple solid solutions, making the total number of phases well below the maximum equilibrium number allowed by the Gibbs phase rule. The solid-solution strengthening mechanism and the structure transformation from fcc to bcc make the alloys have fairly high compressive strength; among them the compressive strength of $Al_{11.1}(TiVCrMnFeCoNiCu)_{88.9}$ alloy reaches 2.431 GPa.

Keywords: High-entropy alloy; Microstructure; Compressive properties

1. Introduction

Conventional strategy for developing new alloys is based on one or two elements as major constituent, and other minor elements as their constituents for the enhancement of definite properties. The main reason for not incorporating multi-principal elements into alloy preparation is the anticipated formation of many intermetallic compounds and complex microstructures, which would make alloys brittle and difficult in processing and analysis [1].

Recently, a new alloy system called "high-entropy alloy" (i.e. HEA) was developed and the cognitive strategy of alloy design was broken through [2,3]. HEA contains multi-elements as its major constituents, and each constituent element in the system could be regarded as a solute atom. To increase the entropy, each major element of the alloy system is in equimolar or near-equimolar ratio.

The microstructure and compressive properties of $Al_x(TiVCrMnFeCoNiCu)_{100-x}$ ($x = 0$, 11.1, 20 and 40 at.%) high-entropy alloys were studied in this paper. Our purpose is, by the research of the new alloys, to investigate its properties and potential applications.

2. Experimental

HEA (i.e.$Ti_{12.5}V_{12.5}Cr_{12.5}Mn_{12.5}Fe_{12.5}Co_{12.5}Ni_{12.5}Cu_{12.5}$) was prepared as intermediate alloy from commercial-purity elements (purity better than 99 wt.%) by medium-frequency induction melting under inert atmosphere. This alloy was then melted with Al (99.7 wt.%) to obtain alloy ingots with nominal composition of $Al_x(HEA)_{100-x}$ ($x = 0$, 11.1, 20 and 40 at.%) alloys by arc melting in a Ti-gettered argon atmosphere. The alloys were remelted four times to improve homogeneity. After that, the ingots were inductively melted in quartz tube under a vacuum (10^{-3} Pa), and then injection cast into a water-cooled copper mould with diameter of 5 mm and length of 70 mm.

The structure of the cylindrical alloys (cross-sectional surface) was characterized by X-ray diffraction (XRD) using a MXP21VAHF diffractometer with Cu Kα radiation. The morphology and composition of as-cast specimens were examined with a LEO-1450 scanning electron microscope (SEM) with energy dispersive spectrometry (EDS). Thin-foil specimens were prepared by mechanical thinning followed by ion milling, and subsequently observed using a JEM-2000 high resolution transmission electron microscope (HRTEM). For compressive tests, samples with 5 mm in diameter and 10 mm in height were prepared and investigated with MTS 809 materials testing machine at room temperature with a strain rate of 1×10^{-4} s^{-1}. A Cambridge S250MK2 scanning electron microscope was

* Corresponding author. Tel.: +86 10 62322160; fax: +86 10 62332508.
E-mail addresses: jxgznd_zyj@yahoo.com.cn, jxgznd_zyj@163.com (Y.J. Zhou), drzhangy@skl.ustb.edu.cn (Y. Zhang).

0921-5093/$ – see front matter © 2006 Elsevier B.V. All rights reserved.
doi:10.1016/j.msea.2006.11.049

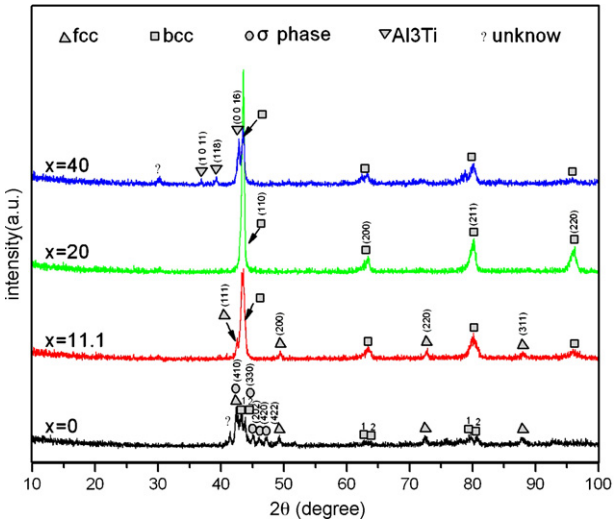

Fig. 1. XRD patterns of $Al_x(HEA)_{100-x}$ alloys.

used to study the fracture surface of the compression test samples.

3. Results

3.1. Structural characterization

The XRD patterns of the as-cast alloys are presented in Fig. 1. The structure of Al_0HEA_{100} alloy is rather complex. Both fcc and bcc solid-solution structures, together with σ phase and a few unknown phases are found in this alloy. The broad diffraction peak at $2\theta = 42–47^\circ$ in its pattern indicates that amorphous phase exists in Al_0HEA_{100} alloy. With the increase of Al content, the number of phases gradually decreases. For $Al_{11.1}HEA_{88.9}$ alloy, except for fcc and bcc reflections, no other phases can be found. From the strongest XRD peak, the lattice parameters of fcc and bcc are estimated to be 0.3673 and 0.2934 nm, respectively. When Al content reaches 20 at.%, only bcc solid-solution structure can be found in the alloy. As Al content increases to 40 at.%, intermetallic phases, such as Al_3Ti and some other unknown ordered phases, present besides bcc solid solution. Thus, the addition of Al makes the alloys gradually transform from fcc into stabilized bcc, but too much Al leads to the precipitation of brittle intermetallic phases such as Al_3Ti.

Fig. 2 shows the SEM backscattered electron images of the alloys. The chemical compositions derived from EDS analysis are listed in Table 1. All the alloys exhibit a typical cast dendrite structure, with the dendrite size and morphology similar to each other. The dendrites are round and irregular with an average primary arm width of 8–14 μm. As shown in Fig. 2(a), the dendrites of Al_0HEA_{100} alloy contain multiphases. For $Al_{11.1}HEA_{88.9}$ alloy, dendrites consist of bcc single phase, while interdendrites exhibit eutectic structure obviously (as shown in Fig. 2(b)), that is, fcc and bcc coexist. For $Al_{20}HEA_{80}$ alloy, both the dendrites and interdendrites are composed of bcc single phase as shown in Fig. 2(c). For the three alloys above, Cu segregates preferentially to the interdendrites, it is reasonable to deduce that the interdendrites are mainly composed of solid solution in which Cu is solvent. The serious Cu segregation should be attributed to the small bonding energies of Cu with other atoms for which Cu is rejected into the interdendrite region. The interdendrites of $Al_{40}HEA_{60}$ alloy show multiphases, both needle-like phase and some other order phases precipitated can be observed in Fig. 2(d). According to XRD and EDS analysis, these phases are identified to be Al_3Ti and an ordered intermetallic phase.

Fig. 3 shows the HRTEM and corresponding selected area inverse fast Fourier transform (IFFT) images of Al_0HEA_{100} alloy. The ordered nanophase (as shown in Fig. 3(b)), inset fast Fourier transform (FFT) image and disordered matrix (as shown in Fig. 3(c)), confirm the existence of nanoparticles and amorphous phase, respectively. It can be seen in Fig. 3(a) that the dispersing nanoparticles are embedded in the amorphous matrix.

3.2. Compressive properties

Fig. 4 shows the true stress–strain curves of room temperature compressive test for the alloys. Both $Al_{11.1}HEA_{88.9}$ and $Al_{20}HEA_{80}$ alloys exhibit fairly high compressive strength, some plastic deformation and slight work hardening capacity. The compressive strength and plastic strain of $Al_{11.1}HEA_{88.9}$ alloy are 2.431 GPa and 0.95%, respectively. As for $Al_{20}HEA_{80}$ alloy, its compressive strength is 2.016 GPa, and plastic strain is 2.35%. Both Al_0HEA_{100} and $Al_{40}HEA_{60}$ alloys exhibit brittle fracture, with compressive strengths of 1.312 and 1.461 GPa, respectively. The Young's modulus (E), yield strength σ_y, com-

Table 1
Chemical compositions of as-cast Al–HEA alloy system (at.%)

Alloy	Region	Al	Ti	V	Cr	Mn	Fe	Co	Ni	Cu
Al_0HEA_{100}	Dendrite	0	23.38	9.78	5.60	9.95	11.22	18.60	15.71	5.77
	Interdendrite	0	1.76	0.37	0.75	22.17	1.13	0.79	8.18	64.86
$Al_{11.1}HEA_{88.9}$	Dendrite	14.48	9.81	17.28	17.32	2.82	12.78	12.38	9.67	3.46
	Interdendrite	4.37	1.14	0.63	0.75	11.71	1.48	1.18	4.19	74.55
$Al_{20}HEA_{80}$	Dendrite	23.61	10.58	11.90	10.94	6.90	10.30	11.53	9.77	4.47
	Interdendrite	20.55	0.55	0.37	0.70	22.28	0.92	0.43	3.74	50.46
$Al_{40}HEA_{60}$	Dendrite	37.97	3.82	19.70	19.96	3.51	6.87	2.59	2.50	3.08
	Interdendrite	51.38	15.02	6.18	3.21	2.01	6.41	7.40	6.45	1.95

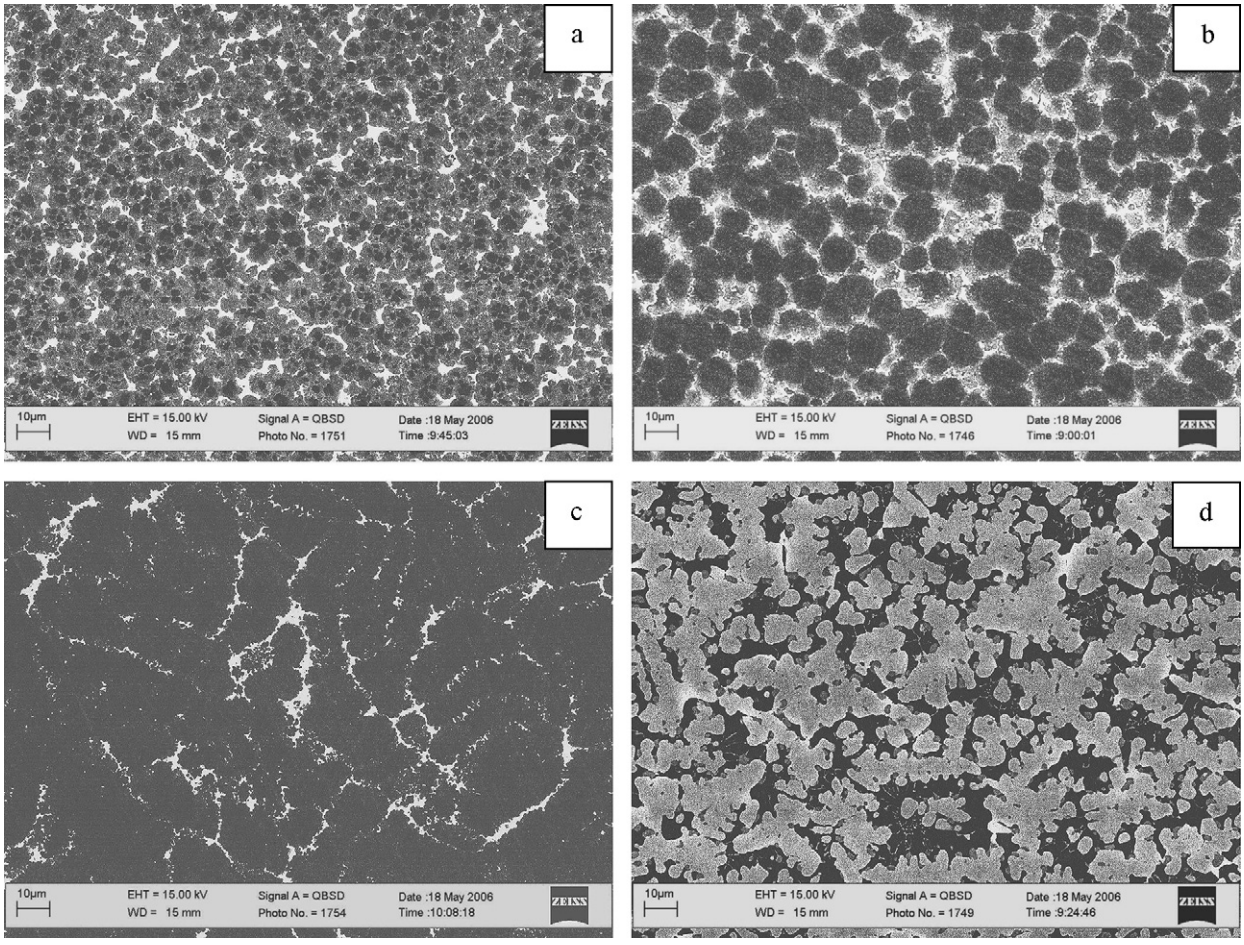

Fig. 2. SEM backscattered electron images of as-cast $Al_x(HEA)_{100-x}$ alloys (x values): (a) 0, (b) 11.1, (c) 20 and (d) 40.

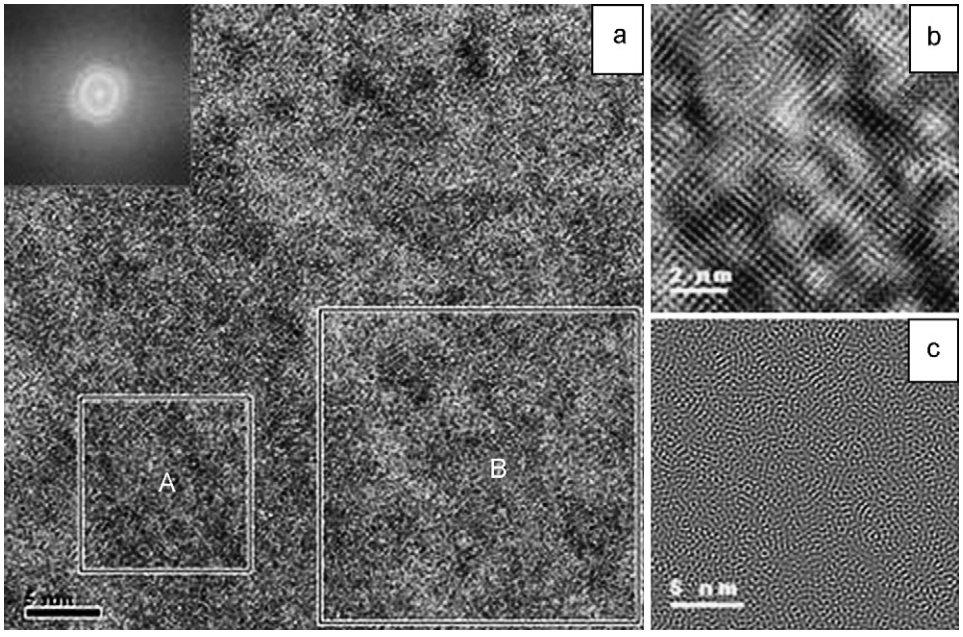

Fig. 3. (a) HRTEM and corresponding selected area IFFT images of Al_0HEA_{100} alloy. IFFT images (b) and (c) indicate region A of nanoparticles and region B of full amorphous matrix, respectively. The inset of (a) shows the FFT image of amorphous matrix.

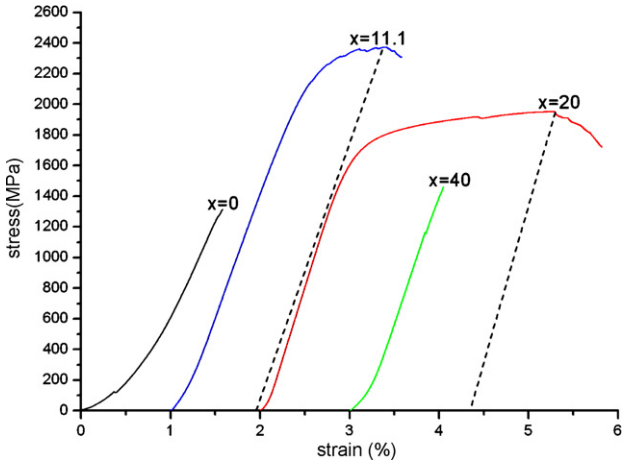

Fig. 4. Compressive true stress–strain curves of $Al_x(HEA)_{100-x}$ alloys.

pressive strength σ_{max} and plastic strain limit ε_p are listed in Table 2.

The fracture surfaces are shown in Fig. 5. For Al_0HEA_{100} alloy, it shows quasi-cleavage facets (as shown in Fig. 5(a)). As multiphases coexist in the structure, the small binding force among these phases makes it lose plasticity at all. The rough facets and river-like patterns in Fig. 5(b) show that the fracture form of $Al_{11.1}HEA_{88.9}$ alloy is typically intercrystalline fracture accompanied by cleavage fracture. On the fracture surface of $Al_{20}HEA_{80}$ alloy, high-density short tear edges and cleavage steps can be observed (as shown in Fig. 5(c)), which was typical feature of quasi-cleavage fracture. The flat fracture surface shown in Fig. 5(d) indicates that $Al_{40}HEA_{60}$ alloy clearly exhibits purely brittle cleavage fracture. Obviously, the precipitation of brittle intermetallic phases like Al_3Ti seriously damages the plasticity of $Al_{40}HEA_{60}$ alloy.

Table 2
Room temperature compressive properties of $Al_x(HEA)_{100-x}$

Alloy	E (GPa)	σ_y (GPa)	σ_{max} (GPa)	ε_p (%)
Al_0HEA_{100}	74.247	1.312	1.312	0
$Al_{11.1}HEA_{88.9}$	164.087	1.862	2.431	0.95
$Al_{20}HEA_{80}$	190.086	1.465	2.016	2.35
$Al_{40}HEA_{60}$	163.208	1.461	1.461	0

Young's modulus (E), yield stress (σ_y), compressive strength (σ_{max}) and plastic strain (ε_p).

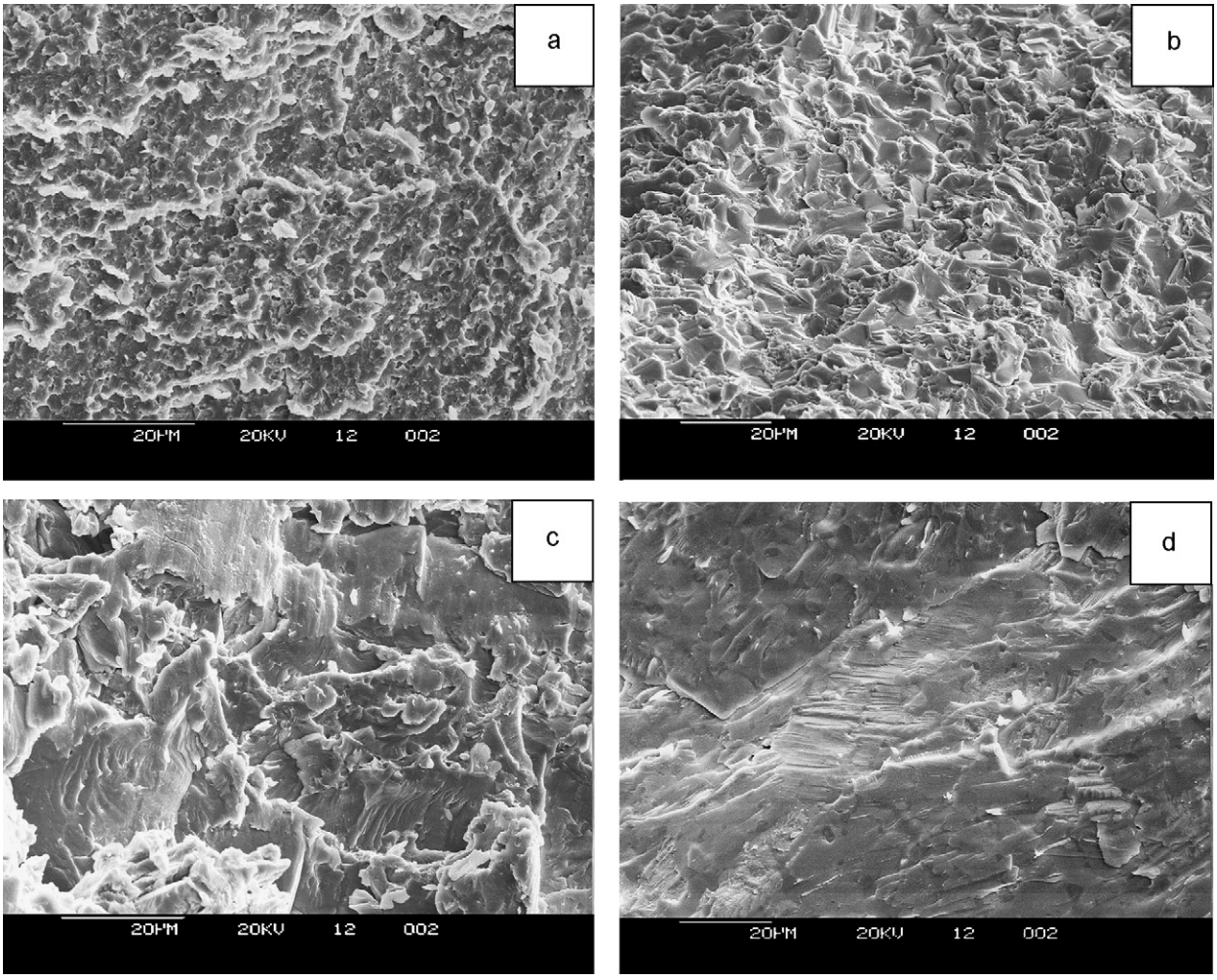

Fig. 5. Scanning electron micrograph of compressive fracture surface of $Al_x(HEA)_{100-x}$ alloys (x value): (a) 0, (b) 11.1, (c) 20 and (d) 40.

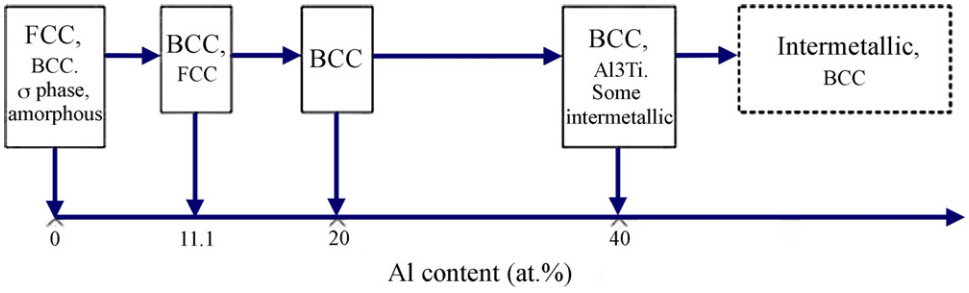

Fig. 6. Schematic illustration of phase transformation with the increase of Al content in $Al_x(HEA)_{100-x}$ alloys. Bigger font indicates main phase, broken line frame shows the prediction.

4. Discussion

According to the Gibbs phase rule: $F = C - P + 1$ (F, degree of freedom; C, number of components; P, number of phases), the maximum number of equilibrium phases in a C component system at constant pressure is: $P = C + 1$. The value of P may even be greater under non-equilibrium condition. The study of conventional alloys also indicates that a large number of intermetallic compounds or other complex ordered phases are expected to form in multicomponent alloy systems [1,4]. However, in this research, simple solid-solution phases like fcc and bcc are superior to intermetallic phases to form in $Al_x(HEA)_{100-x}$ alloys with multi-principal elements, and the total number of phases is well below the maximum equilibrium number allowed by the Gibbs phase rule.

The superiority of simple solid solutions over intermetallic compounds in the alloys is attributed to the effect of the high mixing entropy. Based on the formula of free energy: $G = H - TS$, and Boltzmann's hypothesis between the entropy and the complexity of the system [5], the effect of high mixing entropy is as following: (1) significantly lowers the free energy, thus lowering the tendency to order and segregate, and making it to be more stable at elevated temperature [6–8], (2) relaxes the constraints set by the Hume–Rothery rule between two elements, thus promoting the mutual solubility among multi-principal elements to form substitution solid solutions in alloys [9,10] and (3) balances the lattice strain caused by the solid-solution phenomenon of large atom into the alloy structure, so as to make solid solution more stable than ordered intermetallics, especially at high temperature[11].

The mixing entropy of alloys is as following. The highest value could be attained when $c_1 \approx c_2 \approx \ldots \approx c_i$.

$$S^m_{\text{mix}} = -R\sum_{1}^{i} c_i \ \ln c_i$$

$$\left(\sum_{1}^{i} c_i = 1, \ \ c_i : \text{mole percent of component}\right)$$

Thus, both $Al_{11.1}HEA_{88.9}$ and $Al_{20}HEA_{80}$ alloys, which have higher mixing entropy than Al_0HEA_{100} and $Al_{40}HEA_{60}$ alloys, are composed mainly of simple solid solution and have simpler microstructure than the other two alloys. When Al content increases to 40 at.%, due to the weakening of the effect of high mixing entropy, intermetallic compounds like Al_3Ti precipitate. It is reasonable to deduce that as Al content continuously increases over 40 at.%, intermetallics would have higher fraction or even be the main phase. Fig. 6 is the schematic illustration of phase transformation with the increase of Al content in the alloys.

As "confusion principle" indicates, increasing the number of elements in alloys inhibits nucleation of stable (or metastable) crystalline precipitates and hence facilitates the formation of glass in alloys [12]. The further reason is that a mixture of these elements leads to dense packing in the liquid state, and the resulting stability favors glass formation over crystallization. For Al_0HEA_{100} alloy, dense packing will be attained in local regions due to the proper arrangement of so many components with different atomic size, thus amorphous phase forms and can be seen in these regions.

The compressive strengths of all the alloys are higher than 1.3 GPa, among which $Al_{11.1}HEA_{88.9}$ alloy exhibits the highest compressive strength of 2.431 GPa and some plastic deformation. The reason is mainly related to the solid-solution strengthening mechanism of Al atoms. In the alloys, Al not only has strong binding forces with other elements but also a larger radius than most of the other components, thus both the increased Young's modulus and the large lattice strain effect are significant for alloy strengthening. Besides, the transformation of the crystal structure of the alloys from ductile fcc to strong bcc with the increase of Al content also results in the elevation of compressive strength. At the same time, we should also notice that both the composite structure of multiphases and brittle intermetallics precipitated seriously damage the mechanical properties of the alloys.

5. Conclusion

With the increase of Al content, the number of phases in $Al_x(HEA)_{100-x}$ ($x = 0$, 11.1, 20, 40 at.%) alloys gradually decreases. The composite structures of fcc, bcc, σ phase and amorphous phase are found in Al_0HEA_{100} alloy. For $Al_{20}HEA_{80}$ alloy, both the dendrites and interdendrites are composed of bcc solid-solution structure. As for $Al_{40}HEA_{60}$ alloy, due to the weakening of the effect of high mixing entropy, intermetallic phases such as Al_3Ti precipitate besides bcc phase. The effect of high mixing entropy does facilitate the formation of simple solid solutions in alloys, making the total number of phases well

below the maximum equilibrium number allowed by the Gibbs phase rule. The solid-solution strengthening mechanism and the structure transformation from fcc to bcc make the alloys have fairly high compressive strength; among them the compressive strength of $Al_{11.1}HEA_{88.9}$ alloy is as high as 2.431 GPa.

Acknowledgments

The authors would like to thank X.D. Hui for technical asistance in samples preparation. Authors would like to acknowledge the financial support by the National Natural Science Foundation of China (NNSFC) under the granted No. 50571018, and Program for New Centrury Excellent Talents in University (NCET) of China.

References

[1] A.L. Greer, Nature 366 (1993) 303.
[2] J.W. Yeh, S.K. Chen, S.J. Lin, J.Y. Gan, T.S. Chin, T.T. Shun, C.H. Tsau, S.Y. Chang, Adv. Eng. Mater. 6 (2004) 299.
[3] X.F. Wang, Y. Zhang, Y. Qiao, G.L. Chen, Intermetallics 15 (2007) 357.
[4] Handbook Committee, Metals Handbook, vol. 3, 10th ed., ASM International, Metals Park, OH, 1990, p. 2.25.
[5] R.A. Swalin, in: E. Burke, B. Chalmers, J. AlKrumhansl (Eds.), Thermodynamics of Solids, second ed., John Wiley & Sons, New York, NY, 1991, p. 21.
[6] K.A. Porter, K.E. Easterling, Phase Transformation in Metals and Alloys, Chapman & Hall, New York, NY, 1981, p. 308.
[7] S. Ranganathan, Curr. Sci. 85 (2003) 1404.
[8] F.R. de Boer, Cohesion in metals, in: F.R. de Boer, D.G. Pettifor (Eds.), Transition Metal Alloys, Elsevier, New York, NY, 1988.
[9] R.E. Reed-Hill, R. Abbaschian, Physical Metallurgy Principles, third ed., PWS Publishing Company, Boston, MA, 1994, p. 272.
[10] B. Cantor, I.T.H. Chang, P. Knight, A.J.B. Vincent, Mater. Sci. Eng. A 375–377 (2004) 213.
[11] C.J. Tong, Y.L. Chen, S.K. Chen, J.W. Yeh, T.T. Shun, C.H. Tsau, S.J. Lin, S.Y. Chang, Met. Mater. Trans. A 36A (2005) 881.
[12] X. Gu, L.Q. Xing, T.C. Hufnagel, J. Non-Cryst. Solids 311 (2002) 77.